ZnO-Based Conversion/Alloying Negative Electrodes for Lithium-Ion Batteries: Impact of Mixing Intimacy

*Jakob Asenbauer, Stefano Passerini, and Dominic Bresser**

Conversion/alloying materials, such as transition metal (TM)-doped ZnO, are showing superior performance over pure ZnO due to the presence of the TM, enabling the reversible formation of Li_2O due to the enhanced electronic conductivity within the single particle once being reduced to the metallic state upon lithiation. Herein, the impact of introducing Co as representative TM at the atomic level in ZnO compared with mixtures of nano- and microsized CoO and ZnO is investigated. While even rather simple mixtures provide higher capacities than pure ZnO, an intimate mixing of nanoparticulate CoO and ZnO leads to a further increase due to the more homogeneous dispersion of Co. Nonetheless, the "atomic mixing" via doping still provides the highest capacities—for both nano- and microparticles, thus highlighting the importance of the very fine distribution of Co (and generally the TM) for realizing effective electron conduction pathways to enable the reversible formation of Li_2O.

1. Introduction

Since their commercialization in the 1990s, lithium-ion batteries became the energy storage technology of choice to power portable electronic devices and, more recently, larger scale applications such as plug-in hybrid electric vehicles (PHEV) or electric vehicles (EVs).[1–3] Especially for the latter application, batteries with high power and energy densities are urgently required.[4–6] Since these performance characteristics are majorly defined by the chemistry of the electrode active materials, large efforts have been made to identify and develop suitable alternatives. On the anode side, graphite is the state-of-the-art; yet its theoretical capacity is limited to $372 \, \text{mAh g}^{-1}$ and its sluggish lithiation kinetics prevents fast charging of the battery.[7] Potential alternatives which provide higher specific capacities are alloying, conversion, and conversion/alloying materials—

the latter combining the two different de-/lithiation mechanisms in one single compound.[8] Among the most investigated members of this class are transition metal (TM)-doped zinc oxides (with TM = Fe,[9–14] Co,[15,16] or Mn[17,18]), providing a theoretical specific capacity of almost $1000 \, \text{mAh g}^{-1}$ and good cycling performance, thus clearly outperforming pure ZnO.[9,19] It has been proposed that the "intimacy of mixing" the different metals plays a decisive role in the electrochemical performance.[20] In fact, doping, e.g., ZnO with TMs is essentially equivalent to the mixing of different elements at the atomic level. In this line, a comparative investigation of $NiCo_2O_4$ and a stoichiometric mixture of NiO and Co_3O_4 revealed that electrodes based on the former active material are outperforming those of mixtures.[21] However, it has also been reported that mixing SnO_2, metallic manganese, and graphite particles can as well inhibit Sn coarsening, enabling the reversible formation of Li_2O.[22] Accordingly, the impact of the intimacy of mixing the different metallic elements still requires further investigation.

Herein, we report a comprehensive comparative investigation of Co-doped ZnO, serving as model compound, with a manually ground and ball-milled mixture of CoO and ZnO nano- and microparticles to obtain mixtures at different length scales and of different intimacy to provide an answer on the question how intimate the TM and the alloying element have to be for achieving the reversible formation of Li_2O upon de-/lithiation.

2. Results and Discussion

2.1. Structural and Morphological Characterization

Figure 1a shows the comparison of the X-ray diffraction (XRD) patterns of the nanosized samples, i.e., $Zn_{0.9}Co_{0.1}O^{nano}$, ZnO^{nano}, and CoO^{nano}. Both $Zn_{0.9}Co_{0.1}O^{nano}$ and ZnO^{nano} have a hexagonal wurtzite structure, matching the reference data (PDF 01-071-6424), and do not show any additional reflections, indicating that the introduction of Co into the ZnO crystal lattice has been successful for $Zn_{0.9}Co_{0.1}O^{nano}$.[23] CoO^{nano} shows a phase pure rock-salt cubic structure, matching the reference PDF 00-048-1719. All nanosized samples show rather broad reflections, indicating a small crystallite and/or particle size of the materials. The XRD patterns of the microsized materials ($Zn_{0.9}Co_{0.1}O^{micro}$, ZnO^{micro}, and CoO^{micro}) are shown in Figure 1b. Also in this case all materials reveal the expected

Dr. J. Asenbauer, Prof. S. Passerini, Dr. D. Bresser
Helmholtz Institute Ulm (HIU)
Helmholtzstrasse 11, 89081 Ulm, Germany
E-mail: dominic.bresser@kit.edu

Dr. J. Asenbauer, Prof. S. Passerini, Dr. D. Bresser
Karlsruhe Institute of Technology (KIT)
P.O. Box 3640, 76021 Karlsruhe, Germany

The ORCID identification number(s) for the author(s) of this article can be found under https://doi.org/10.1002/ente.202001084.

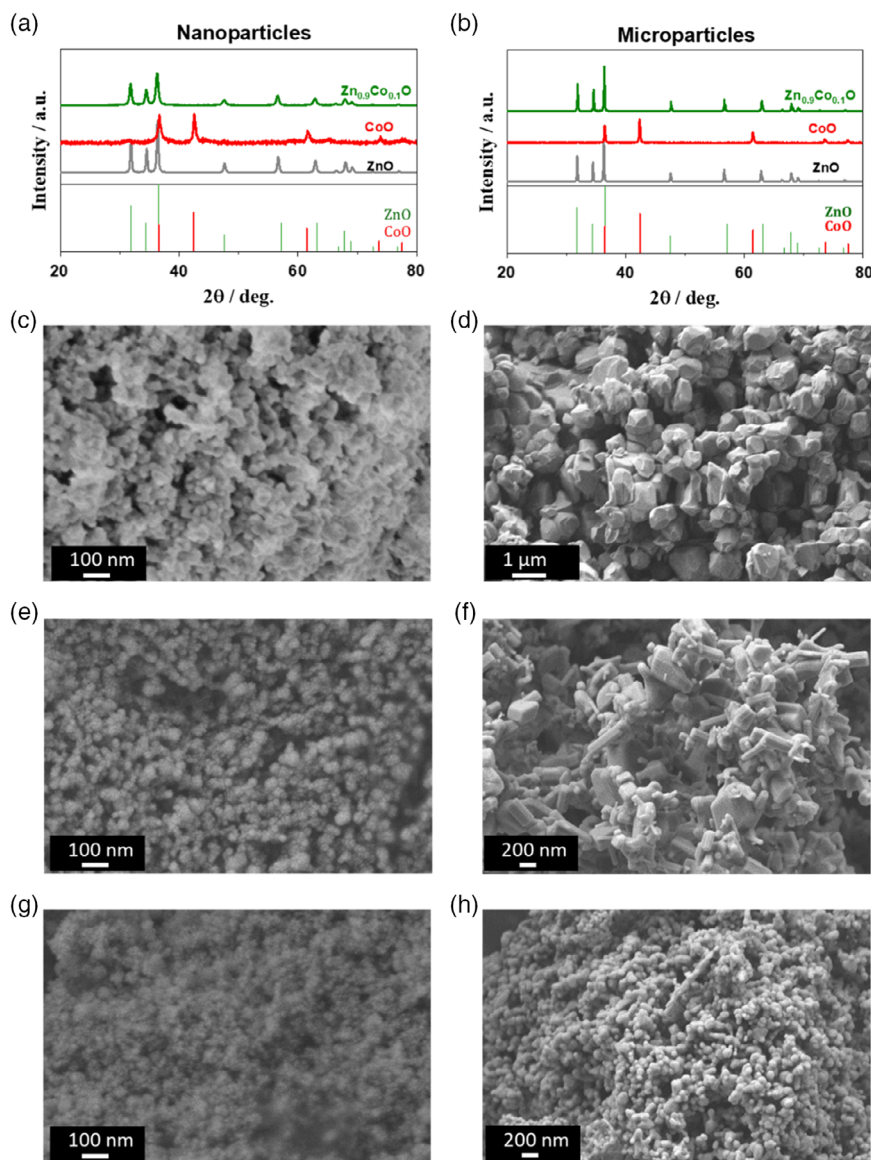**Figure 1.** a) Comparison of the XRD patterns for nanosized $Zn_{0.9}Co_{0.1}O^{nano}$ (in green), CoO^{nano} (in red), and ZnO^{nano} (in gray). b) Comparison of the XRD patterns for microsized $Zn_{0.9}Co_{0.1}O^{micro}$ (in green), CoO^{micro} (in red), and ZnO^{micro} (in gray). The PDF references 01-071-6424 for wurtzite ZnO (in green) and 00-048-1719 for rock-salt CoO (in red) are provided in the bottom in both cases. SEM images of c) $Zn_{0.9}Co_{0.1}O^{nano}$, d) $Zn_{0.9}Co_{0.1}O^{micro}$, e) ZnO^{nano}, f) ZnO^{micro}, g) CoO^{nano}, and h) CoO^{micro}.

(phase pure) crystalline structures, i.e., the wurtzite structure for $Zn_{0.9}Co_{0.1}O^{micro}$ and ZnO^{micro} and the rock-salt cubic structure for CoO^{micro}. The narrow shape of the reflections indicates a larger crystallite and/or particle size compared with the nanosized materials. The subsequently conducted scanning electron microscopy (SEM) analysis of the different materials reveals a particle size of about 30 nm for $Zn_{0.9}Co_{0.1}O^{nano}$ (Figure 1c), around 0.2–1 µm for $Zn_{0.9}Co_{0.1}O^{micro}$ (Figure 1d), ≈30 nm for ZnO^{nano} (Figure 1e), ≈0.2–0.6 µm for ZnO^{micro} (Figure 1f), about 20 nm for CoO^{nano} (Figure 1g), and 0.1 µm for CoO^{micro} (Figure 1h—in fact, strictly speaking the particle size is more in the submicron range, but significantly larger than CoO^{nano}). These findings are in general agreement with the XRD analysis and the general trend for the broadening of the reflections, suggesting that the particles are essentially monocrystalline. In addition, all materials are composed of roughly spherical particles; just for ZnO^{micro} a mixture of larger essentially spherical particles (≈600 nm) and relatively smaller rods (≈50–200 nm in diameter and several hundred nm in length) is observed. In fact, the simultaneous presence of such rod-shaped particles is frequently observed for pure ZnO and has been assigned to the generally preferred crystal growth along the (001) direction.[24,25]

For the comparison of doped and mixed samples, stoichiometric mixtures (molar ratio of 90:10) of nanosized and microsized ZnO and CoO were prepared. For the mixing process two different procedures were used to vary the intimacy of the resulting composite: 1) manual grinding in an agate mortar for 10 min,

yielding 90ZnO:10CoO^{nano} and 90ZnO:10CoO^{micro}, and 2) manual grinding for 10 min followed by dry planetary ball-milling for 2 h, yielding 90ZnO:10CoO^{nano}-BM and 90ZnO:10CoO^{micro}-BM. The latter approach was chosen to overcome potential agglomeration effects commonly occurring for sufficiently small particles (especially when approaching and/or entering the nanoscale) due to the increasing importance of the particle surface and, thus, the surface free energy.[26,27] These composites were also studied via XRD to rule out any potential structural degradation and/or reaction among the two single compounds, particularly for the ball-milled materials. The results are shown in **Figure 2**a for 90ZnO:10CoO^{nano}(-BM) and Figure 2b for 90ZnO:10CoO^{micro} (-BM). All diffractograms show a combination of wurtzite ZnO and rock-salt CoO without any additional phase, confirming that neither the manual grinding nor the ball-milling induced any chemical reaction and/or structural degradation.

2.2. Comparative Electrochemical Characterization

Following the goal of this work, i.e., the investigation of the impact of the mixing intimacy (at the atomic scale vs the nanoscale vs the microscale) on the electrochemical behavior, electrodes were prepared using the different active materials and composites, as also schematically shown in **Figure 3**a. All electrochemical tests were performed in half-cell configuration, i.e., versus metallic lithium as counter electrode. Figure 3b shows

Figure 2. a) Comparison of the XRD patterns recorded for 90ZnO:10CoO^{nano} (in blue) and 90ZnO:10CoO^{nano}-BM (in red) as well as b) the XRD patterns recorded for 90ZnO:10CoO^{micro} (in blue) and 90ZnO:10CoO^{micro}–BM (in red). The PDF references 01-071-6424 for wurtzite ZnO (in green) and 00-048-1719 for rock-salt CoO (in red) are provided in the bottom.

the plot of the specific capacity of electrodes based on Zn$_{0.9}$Co$_{0.1}$O^{nano}, 90ZnO:10CoO^{nano}, 90ZnO:10CoO^{nano}-BM, and ZnO^{nano} upon constant current cycling at C/20 (50 mA g^{-1}) versus the cycle number. Zn$_{0.9}$Co$_{0.1}$O^{nano} shows the highest reversible capacity of around 900 mAh g^{-1} during the first 15 cycles before it starts to gradually increase to around 1000 mAh g^{-1} during the next 20 cycles and after it slightly decreases again to about 900 mAh g^{-1} at the 50th cycle. The electrodes based on 90ZnO:10CoO^{nano}-BM show the second-highest reversible capacity of the four nanosized materials, though substantially lower specific capacities than the doped material. Its reversible capacity is 830 mAh g^{-1} in the first cycle, which decreases to about 450 mAh g^{-1} during the first ten cycles and then remains relatively stable. 90ZnO:10CoO^{nano} and ZnO^{nano} show an initial capacity of 780 and 710 mAh g^{-1}, respectively, which decreases during the first 15 cycles to a stable value of 350 and 250 mAh g^{-1}. Accordingly, the general trend concerning the stabilized reversible capacity follows the order Zn$_{0.9}$Co$_{0.1}$O^{nano} ≫ 90ZnO:10CoO^{nano}-BM > 90ZnO:10CoO^{nano} > ZnO^{nano}. This general trend is observed also for the microsized particles, i.e., Zn$_{0.9}$Co$_{0.1}$O^{micro} ≫ 90ZnO:10CoO^{micro}-BM > 90ZnO:10CoO^{micro} > ZnO^{micro*} (Figure 3c). In more detail, electrodes based on Zn$_{0.9}$Co$_{0.1}$O^{micro} show the highest reversible specific capacity of ≈850 mAh g^{-1} in the first cycle, which subsequently decreases to a stable value of about 650 mAh g^{-1}. The initial capacity of 90ZnO:10CoO^{nano}-BM, 90ZnO:10CoO^{nano}, and ZnO^{nano} is around 930, 930, and 910 mAh g^{-1}, which gradually decreases to about 470, 440, and 310 mAh g^{-1}, respectively, during the first 20 cycles. For a more in-depth discussion of the electrochemical behavior, the evolution of the corresponding dis-/charge profiles for the 20th–30th cycle (i.e., after the capacity has stabilized) is shown in Figure 3d for the nanosized materials/composites and in Figure 3e for the microsized materials/composites. The voltage profiles of Zn$_{0.9}$Co$_{0.1}$O^{nano} and ZnO^{nano} reveal the same shape as reported in an earlier study.[15] Specifically, upon delithiation a neat separation is observed between the dealloying reaction occurring at lower potentials (up to about 1.25/1.3 V) and the subsequent sloped plateau (at around 1.5 V) for the reconversion reaction in the case of Zn$_{0.9}$Co$_{0.1}$O^{nano}. This latter is essentially absent for ZnO^{nano} due to the irreversibility of the conversion reaction for this material. In fact, also the dealloying capacity is lower for ZnO^{nano}, highlighting the beneficial impact of the TM doping on both mechanisms. The voltage profiles of 90ZnO:10CoO^{nano} show the characteristic profile of ZnO, as apparent from the essentially perfect overlap at low potentials, and some extra capacity at elevated potentials, related to the reconversion reaction of CoO^{nano}[28] (see also Figure S1a, Supporting Information, for comparison). The dis-/charge profiles of 90ZnO:10CoO^{nano}-BM present intermediate features between 90ZnO:10CoO^{nano} and Zn$_{0.9}$Co$_{0.1}$O^{nano}, thus demonstrating the impact of the different intimacy of mixing, i.e., the greater the intimacy the higher the capacity and the better the reversibility of the alloying and conversion reactions. This general trend is even more apparent when comparing the differential capacity plots, exemplarily shown for the 15th cycle in Figure 3e. The electrodes based on Zn$_{0.9}$Co$_{0.1}$O^{nano} show a broad cathodic peak centered at 0.95 V (corresponding to the conversion reaction) and a sharp cathodic peak at around 0 V (corresponding to the alloying reaction). During the delithiation, it shows a broad anodic peak at about
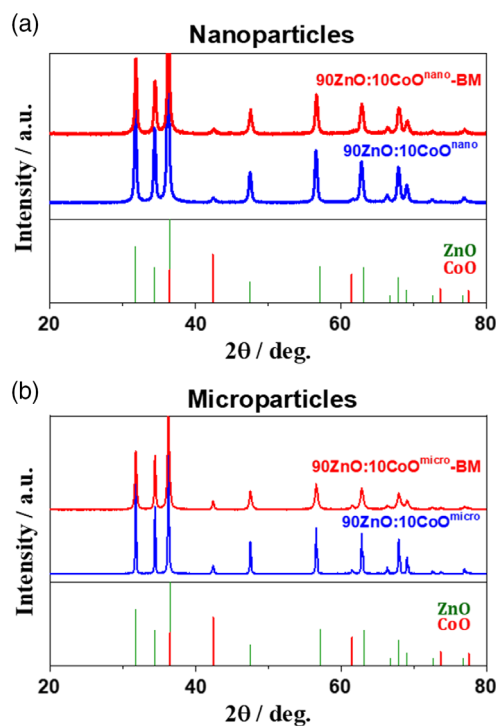
ADVANCED
SCIENCE NEWS

www.advancedsciencenews.com

Energy Technology
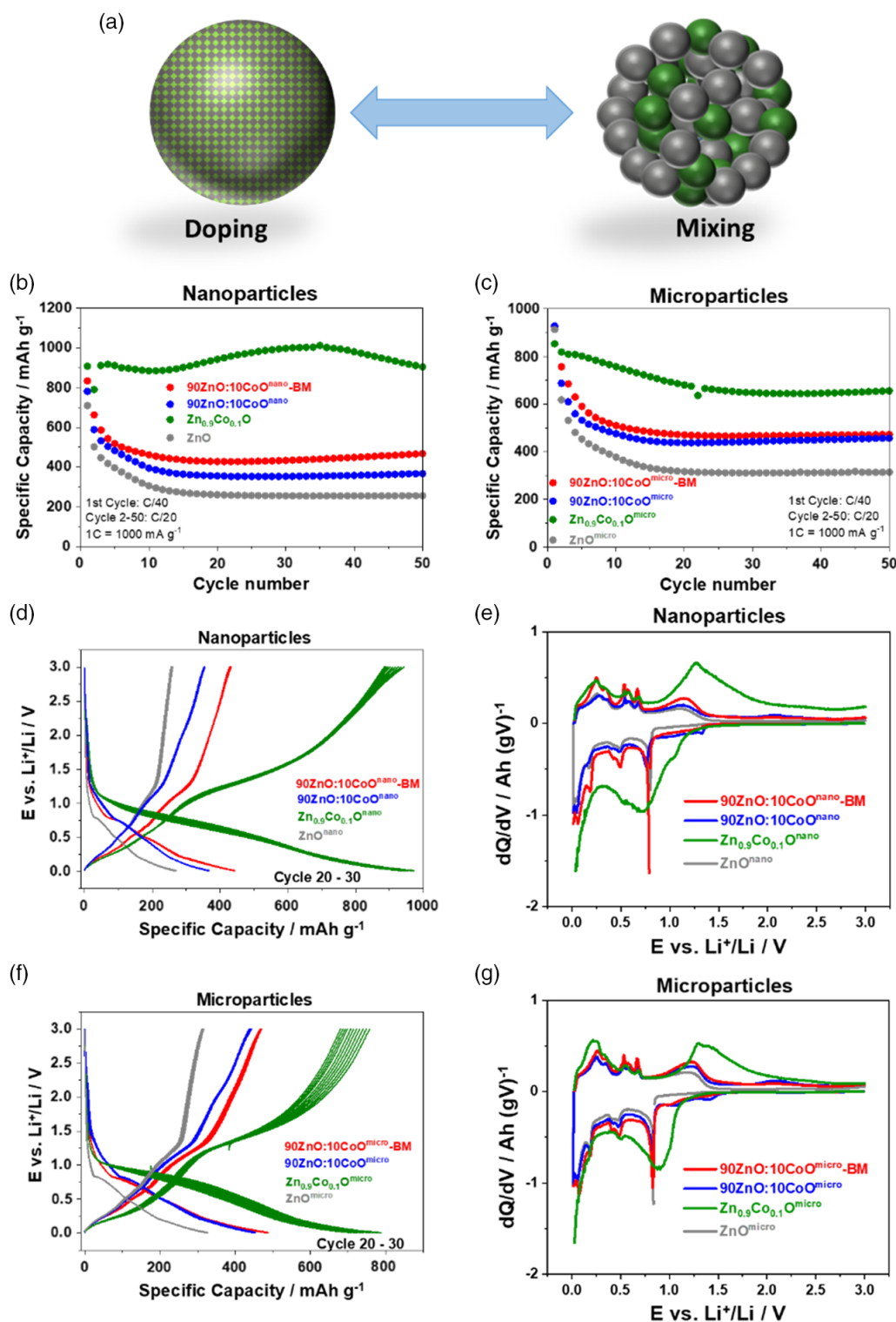Generation, Conversion, Storage, Distribution

www.entechnol.de

Figure 3. a) Schematic illustration of the Co-doped ZnO and the ZnO/CoO composites. Electrochemical characterization of nanosized and microsized $Zn_{0.9}C_{0.1}O$, 90ZnO:10CoO, 90ZnO:10CoO-BM, and ZnO in half-cells via galvanostatic cycling (fitsy cycle at C/40, following cycles at C/20; cutoff voltages: 0.01 and 3.0 V): b,c) plot of the reversible specific capacity (i.e., upon delithiation) for b) the nanosized materials/composites and c) the microsized materials/composites. d) The corresponding dis-/charge profiles for the nanosized materials/composites for the 20th–30th cycle at C/20 and e) the plot of the differential capacity for the 15th cycle. f) The corresponding dis-/charge profiles for the microsized materials/composites for the 20th–30th cycle at C/20 and g) the plot of the differential capacity for the 15th cycle.

0.25 V and three peeks at 0.54, 0.58, and 0.68 V, which correspond to the dealloying reaction, and a very broad anodic peak centered at 1.3 V for the reconversion reaction. The peaks for the ZnO/CoO composites are all much sharper, indicating a larger crystallite size of the relevant crystals being formed during the initial conversion reaction. Moreover, the intensity of the reconversion peak is much lower, reflecting the substantially limited reconversion reaction. ZnO^{nano} shows essentially the same features with a sharp cathodic peak at 0.8 V, two peaks at 0.5 and 0.42 V, as well as one peak at 0.18 V and one peak at around 0.05 V, as characteristic for pure ZnO,[15] though with a further decreased intensity. Upon delithiation, two anodic peaks at 0.25 and 0.35 V and three sharp peaks at 0.45, 0.60, and 0.67 V are observed, related to the dealloying reaction, and a broad peak centered at 1.1 V, which is attributed to the partially reversible reoxidation to ZnO.[15] Compared with the two composites, however, there are a few fine differences. The differential capacity plot of $90ZnO:10CoO^{nano}$ reveals two additional (low-intensity) cathodic peaks at 1.3 and 1.0 V and a broad anodic peak centered at 2.1 V. These additional peaks correspond to the reversible conversion reaction of CoO^{nano}[28] (see also Figure S1b, Supporting Information). Accordingly, the material behaves as a "simple" composite, i.e., it shows the sum of the characteristic peaks for both components ZnO^{nano} and CoO^{nano} and an almost perfect overlap for the ZnO^{nano}-related features. This is a little different for $90ZnO:10CoO^{nano}$-BM. The peaks attributed to ZnO^{nano} appear as well as the same position and the overall shape of the peaks is the same. Nevertheless, the peaks at lower potentials (related to the de-/alloying reaction) are characterized by a significantly higher intensity and the same is observed for the anodic peak at about 1.1 V. Accordingly, the interaction between the two components is enhanced due to the more intimate mixing by applying also a ball-milling step for the composite preparation.

In summary, apart from the general trend concerning the intensity, which is directly correlated to the specific capacity, the most intriguing finding is the extensive broadening of the peaks in the case of the doped material, highlighting the nanocrystallinity of the different electrochemically active phases formed upon lithiation and delithiation.[15] The second important finding is that the position and shape of the peaks recorded for the ball-milled composite are essentially the same as for ZnO^{nano} and the nonball-milled composite, while the intensity of the peaks is higher. This indicates that the crystallite size of the electrochemically active phases formed upon de-/lithiation is not affected by the more intimate mixing and that the increase in capacity is rather caused by enhanced kinetics—presumably due to the better distribution of the metallic cobalt formed during discharge.[29,30]

The dis-/charge profiles recorded for the microsized materials and composites show basically the same trend as the nanosized ones, though less pronounced (Figure 3f). The capacity is slightly less stable for all materials/composites, especially for $Zn_{0.9}Co_{0.1}O^{micro}$, and lower than for the nanosized materials —especially with regard to the contribution of the conversion reaction. Remarkably, the additional ball-milling step appears less effective in this case, as the increase in capacity of $90ZnO:10CoO^{micro}$-BM over $90ZnO:10CoO^{micro}$ is less—in the low and high voltage region—while the improvement of $90ZnO:10CoO^{micro}$ compared with ZnO^{micro} is more pronounced for the microsized materials and composites.

$90ZnO:10CoO^{micro}$ is benefitting specifically from the additional capacity in the high voltage region upon delithiation, which originates (at least in part) from the reconversion of CoO^{micro}[28] (see also Figure S1c and S1d, Supporting Information). The differential capacity plots (Figure 3g) corroborate these findings and the general trend observed also for the nanosized materials and composites, including the slightly higher intensity of the peaks at low potentials for $90ZnO:10CoO^{micro}$-BM in comparison with $90ZnO:10CoO^{micro}$.

2.3. Operando XRD and Ex Situ SEM/Focused Ion Beam/Energy-Dispersive X-Ray Spectroscopy

To further elucidate the impact of mixing ZnO with CoO, we performed an *operando* XRD analysis for $90ZnO:10CoO^{nano}$-BM during the first de-/lithiation. For this purpose, an electrode based on $90ZnO:10CoO^{nano}$-BM was lithiated from open-circuit voltage (OCV) to 0.01 V and subsequently delithiated up to 3.0 V with a specific current of $50\,\mathrm{mA\,g^{-1}}$. The results are shown in **Figure 4**. Figure 4a shows the contour plot of the *operando* XRD measurement and the corresponding voltage profile is shown in Figure 4b. Following the changes observed for the corresponding diffractograms, the lithiation reaction can be divided into three different regions (A, B, and C; shown also as close-ups in Figure 4c–e). In region A (scans 1–10; Figure 4c), the voltage gradually decreases until the first (short) plateau at around 0.5 V is reached. In this region, the intensity of the wurtzite-related reflections remains essentially unchanged. Simultaneously, the (200) reflection of the CoO phase at 42.3° is decreasing and completely vanishes with the tenth scan, indicating the formation of Li_2O and Co^0.[29,30] Subsequently, in region B (scans 11–44; Figure 4d), the main reflections of the ZnO phase disappear and a new reflection appears at 43.2°, corresponding to the formation of metallic Zn^0(PDF 00-004-0831). Beginning from scan 28, three new reflections are observed at 37.3°, 41.3°, and 42.8°, which are assigned to the formation of a Li_xZn (with $x \ll 1$) alloy.[15] Simultaneously with the formation of the alloy, the reflections for ZnO and Zn^0 start to decrease and completely vanish at the end of region B. In region C (scans 45–57; Figure 4e), the intensity of the 37.3° and 42.8° reflections is gradually decreasing and a new reflection at 41.4°, related to the LiZn alloy (PDF 03-065-3016), is observed. Its intensity is continuously increasing while shifting to slightly lower 2θ values—the latter effect indicates an increase in lithium content.[9,31] The subsequent delithiation reaction can be divided into two regions (D and E). In region D (scans 58–66; Figure 4f), the LiZn reflection decreases in intensity and the reflections corresponding to the Li_xZn phase at 37.3° and 42.8° reappear, indicating for the reversibility of the alloying reaction. At the end of region D (scan 66), only the reflections of Li_xZn are left, which vanish abruptly at the beginning of region E (scans 66–79; Figure 4g). In scan 67, only the reflections of the metallic Zn^0 phase at 36.4°, 39.0°, and 43.4° are still observed. Upon further delithiation, the intensity of the Zn^0-related reflections is slightly decreasing, indicating a partial reoxidation of the metallic zinc; however, only to a limited extend. In fact, at the end of region E (i.e., at 3.0 V), the intensity of the Zn^0-reflections is still rather high. In addition, no indication of reoxidized cobalt was
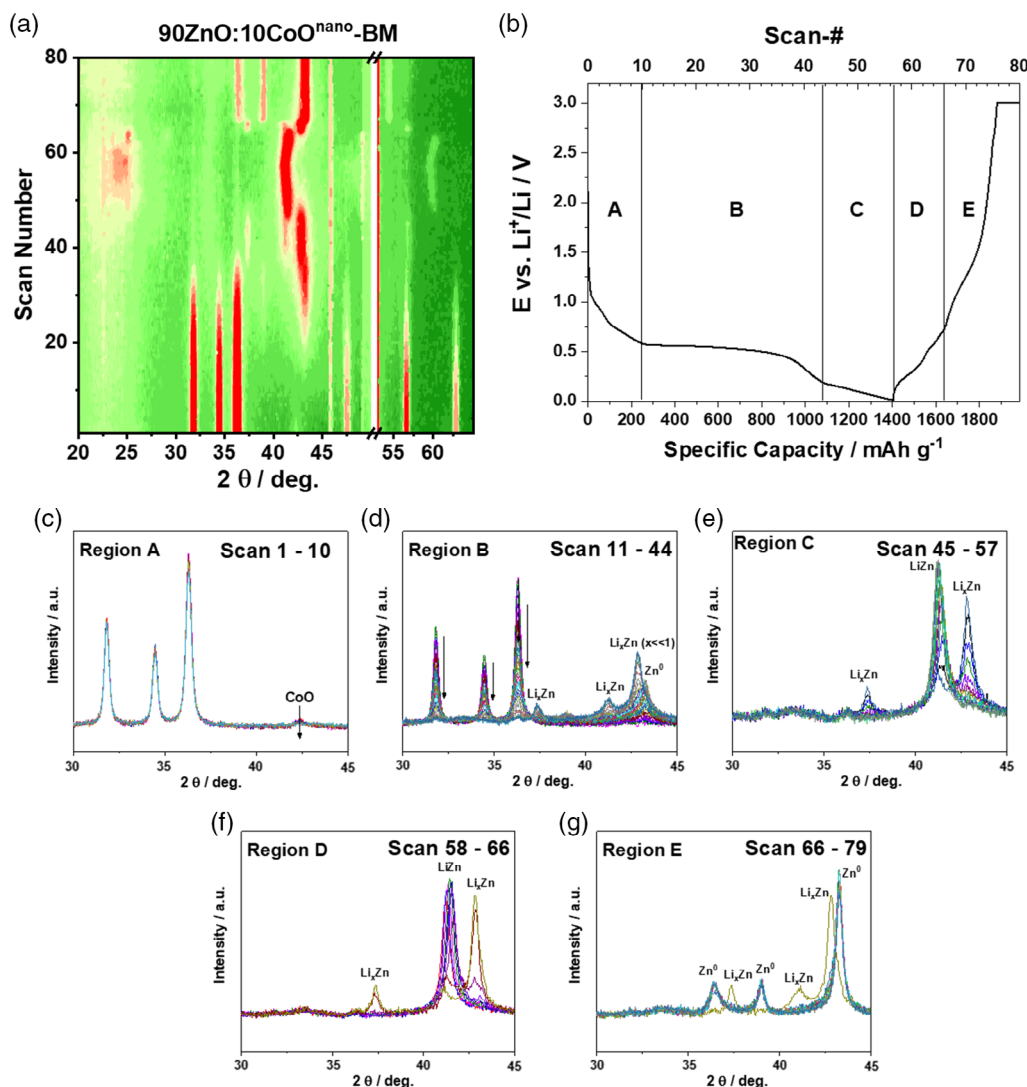
Figure 4. Operando XRD analysis of 90ZnO:10CoO^{nano}-BM in half-cell configuration during galvanostatic lithiation and delithiation (C/20; cutoff voltages: 0.01 and 3.0 V): a) contour plot of the continuously recorded diffractions patterns; b) the corresponding dis-/charge profile, separated in five different regions (A–E); c–g) close-ups of the diffractions patterns for the five different regions indicated in (b).

observed, which is not surprising though, given the nanocrystallinity or quasi-amorphous state of the metallic cobalt. Indeed, this finding is in agreement with previous studies on nanosized CoO.[28,30]

Overall, these results reveal that the reaction mechanism of ZnO^{nano} in 90ZnO:10CoO^{nano}-BM is essentially the same as for pure nanosized ZnO[15]—or in other words, the presence of Co appears to have a negligible effect on the general reaction mechanism in the first cycle apart from the slightly increased reversibility of the conversion reaction (Figure S2, Supporting Information). Differently, the presence of cobalt in Zn$_{0.9}$Co$_{0.1}$O has a much greater impact in terms of a substantially reduced size of the different phases formed upon lithiation and delithiation and, especially, a dramatically enhanced reversibility of the conversion reaction.[15] These findings further corroborate the aforementioned conclusion that the capacity improvement observed for 90ZnO:10CoO^{nano}-BM

compared with ZnO^{nano} is different from the doped material. The cobalt metal resulting from the reduced CoO in the composite certainly increases the electronic conductivity within the electrode coating layer, resulting in improved kinetics for the subsequent lithiation reactions. Following, the reconversion of Co^0 into CoO only occurs at rather high potentials (above 2.0 V). Thus, it is present throughout large parts of the reoxidation of Zn^0 to ZnO (see Figure 3e and Figure S1a, Supporting Information). Thereby, the metallic cobalt may potentially serve as an additional "conductive additive" within the electrode, with the additional ball-milling step enhancing its dispersion.

To confirm this assumption, we performed a comparative focused ion beam (FIB)/SEM/energy-dispersive X-ray spectroscopy (EDX) analysis of the cross section of 90ZnO:10CoO^{nano}-BM and 90ZnO:10CoO^{nano} electrodes (**Figure 5**). Specifically, the magnification of selected areas of the cross section reveals
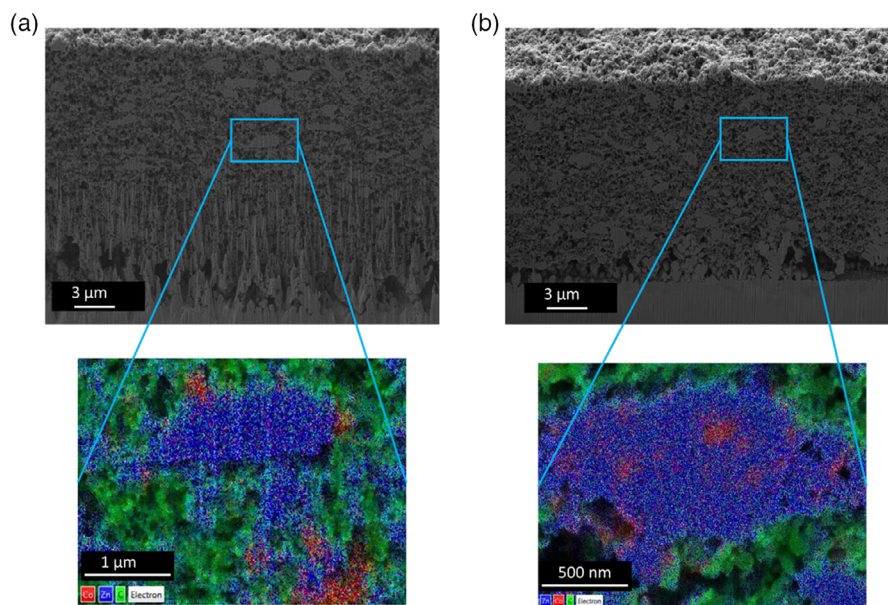
Figure 5. SEM images of FIB-derived cross sections of electrodes based on a) 90ZnO:10CoO^{nano} and b) 90ZnO:10CoO^{nano}-BM. For both electrodes, an additional EDX analysis was performed for a selected area with Zn, Co, and C being colored blue, red, and green, respectively.

that the two components are present in the form of agglomerates, which are smaller for CoO (Co is colored red) and larger for ZnO (Zn is colored blue)—presumably as a result of the 9:1 ratio. The decisive difference, however, is the dispersion of these smaller CoO clusters within the larger ZnO agglomerates in the case of 90ZnO:10CoO^{nano}-BM (Figure 5b), while the CoO clusters and the ZnO agglomerates remain separated in the case of 90ZnO:10CoO^{nano} (Figure 5b).

3. Conclusion

The comparative characterization of Co-doped ZnO, differently mixed ZnO/CoO composites and pure ZnO, reveals that the intimacy of mixing (decreasing in the order $Zn_{0.9}Co_{0.1}O \gg$ 90ZnO:10CoO^{nano}-BM > 90ZnO:10CoO^{nano}) is decisive for the electrochemical performance with regard to the reversibility of the alloying and the conversion reactions. While confining the electrochemically active phases formed upon lithiation and delithiation to the (sub-)nanocrystalline level plays an important role, the homogeneous distribution of the TM, ensuring a percolating electronically conductive network within the electrode, is another important factor. Thus, the better its distribution, the higher the reversibility of the two reaction mechanisms. Given the large number of publications reporting the investigation of composite materials, these findings shed light into what is commonly referred to as "synergistic effect" in such studies and, thus, contribute to a better understanding of the underlying phenomena.

4. Experimental Section

Material Synthesis and Characterization: Nanosized ZnO (ZnO^{nano}) was synthesized according to an earlier reported procedure[9] by dissolving zinc(II) gluconate hydrate (ABCR) in a 1.2 M aqueous sucrose solution

to reach a zinc concentration of 0.2 M. The water was evaporated at 160 °C and the remaining solid material was calcined at 450 °C for 3 h under ambient atmosphere (heating rate: 3 °C min^{-1}). Nanosized $Zn_{0.9}Co_{0.1}O$ ($Zn_{0.9}Co_{0.1}O^{nano}$) was synthesized according to Mueller et al.[15] In brief, zinc(II) gluconate hydrate (ABCR) and cobalt(II) gluconate hydrate (ABCR) were dissolved in a 1.2 M aqueous sucrose solution in the required stoichiometric ratio to reach a total metal concentration of 0.2 M. The water was evaporated at 160 °C and the remaining precursor was calcined at 400 °C for 3 h under ambient atmosphere (heating rate: 3 °C min^{-1}). Microsized $Zn_{0.9}Co_{0.1}O$ ($Zn_{0.9}Co_{0.1}O^{micro}$) was prepared by manually grinding 1 g of the as-synthesized $Zn_{0.9}Co_{0.1}O^{nano}$ powder in an agate mortar, pressing the resulting powder into a pellet at 5 t for 1 min and sintering this pellet at 1000 °C for 3 h under ambient atmosphere (heating rate: 3 °C min^{-1}). Nanosized CoO (CoO^{nano}) (US Research Nanomaterials), microsized ZnO (ZnO^{micro}) (Alfa Aesar), and microsized CoO (CoO^{micro}) (VWR International) were used as received. The crystal structure of the materials was investigated by powder XRD using a Bruker D8 Advance diffractometer (Cu Kα radiation, $\lambda = 0.154$ nm) within a 2θ range of 20–80°. SEM was performed with a Zeiss Crossbeam 340 field-emission electron microscope.

Electrode Preparation, Cell Assembly, and Electrochemical Characterization: For the electrode preparation, the active material and carbon black (Super C65, Imerys) were added to a 1.25 wt% solution of sodium carboxymethyl cellulose (CMC; Dow Wolff Cellulosics) in ultrapure water. The dry composition of all electrodes was 75 wt% of the active material, 20 wt% carbon black, and 5 wt% CMC. The mixture was then homogenized by planetary ball-milling (Pulverisette 4, Fritsch) for 2 h. Subsequently, the slurry was cast on dendritic copper foil (Schlenk) with a wet film thickness of 120 µm by a laboratory-scale doctor blade. The resulting electrode sheets were dried at 80 °C for 5 min, before they were dried overnight at room temperature. Prior to the electrochemical testing, disc electrodes with a diameter of 12 mm were cut and dried under vacuum at 120 °C for 12 h.

The electrochemical characterization was performed in two-electrode coin cells (Hohsen). The cells were assembled in an argon-filled glove box (MBraun) with an oxygen and water content below 0.1 ppm. A sheet of glass fiber fleece (Whatman, GFD), drenched with 150 µL of the electrolyte (1 M LiPF$_6$ in EC:DMC 1:1 w/w), served as the separator. Battery-grade Li metal (Honjo) was used as counter electrode. Galvanostatic

**ADVANCED
SCIENCE NEWS**
www.advancedsciencenews.com

Energy Technology
Generation, Conversion, Storage, Distribution

www.entechnol.de

cycling was performed at 20 °C using a Maccor battery tester 4300. A dis-/charge rate of 1 C corresponds to a specific current of 1000 mA g^{-1} based on the mass of the active material or composite.

Operando XRD: *Operando* XRD upon galvanostatic cycling was performed using a self-designed two-electrode cell.[32] The electrode slurry (with the same composition as mentioned earlier) was homogenized by manual grinding and cast on a beryllium (Be) disc, which served simultaneously as the "window" for the X-ray beam and the current collector. The coated Be disc was dried for 4 h at room temperature and at 60 °C under vacuum for 12 h. Metallic lithium was used as the counter electrode and glass fiber fleeces (diameter: 19 mm), drenched with 300 μL of the electrolyte (1 M LiPF$_6$ in EC:DMC 1:1 w/w), served as the separator. The diffractograms were recorded in a 2θ range of 20–65°. Galvanostatic cycling was performed at room temperature using a VMP SP-200 single-channel potentiostat (Biologic).

SEM/FIB EDX Analysis: FIB milling combined with SEM and EDX was performed utilizing a Zeiss Crossbeam 340 field-emission electron microscope equipped with a Capella FIB with a gallium ion source and an Oxford Instruments X-MaxN EDX spectrometer. To avoid sample damage and curtaining, low currents were chosen for milling (1.5 nA) and polishing (50 pA) the cross sections, applying an acceleration voltage of 30 kV.

Supporting Information

Supporting Information is available from the Wiley Online Library or from the author.

Acknowledgements

Conflict of Interest

The authors declare no conflict of interest.

Keywords

[1] M. Marinaro, D. Bresser, E. Beyer, P. Faguy, K. Hosoi, H. Li, J. Sakovica, K. Amine, M. Wohlfahrt-Mehrens, S. Passerini, *J. Power Sources* **2020**, *459*, 228073.
[2] A. Mauger, C. M. Julien, *Ionics (Kiel)* **2017**, *23*, 1933.
[3] A. Eftekhari, *ACS Sustainable Chem. Eng.* **2019**, *7*, 5602.
[4] R. Mukherjee, R. Krishnan, T.-M. Lu, N. Koratkar, *Nano Energy* **2012**, *1*, 518.
[5] M. Li, J. Lu, Z. Chen, K. Amine, *Adv. Mater.* **2018**, *30*, 1800561.
[6] M. Armand, P. Axmann, D. Bresser, M. Copley, K. Edström, C. Ekberg, D. Guyomard, B. Lestriez, P. Novák, M. Petranikova, *J. Power Sources* **2020**, *479*, 228708.
[7] J. Asenbauer, T. Eisenmann, M. Kuenzel, A. Kazzazi, Z. Chen, D. Bresser, *Sustain. Energy Fuels* **2020**, *4*, 5387.
[8] D. Bresser, S. Passerini, B. Scrosati, *Energy Environ. Sci.* **2016**, *9*, 3348.
[9] D. Bresser, F. Mueller, M. Fiedler, S. Krueger, R. Kloepsch, D. Baither, M. Winter, E. Paillard, S. Passerini, *Chem. Mater.* **2013**, *25*, 4977.
[10] F. Mueller, A. Gutsche, H. Nirschl, D. Geiger, U. Kaiser, D. Bresser, S. Passerini, *J. Electrochem. Soc.* **2016**, *164*, A6123.
[11] L. Cabo-Fernandez, D. Bresser, F. Braga, S. Passerini, L. J. Hardwick, *Batter. Supercaps* **2019**, *2*, 168.
[12] D. Neena, M. Humayun, W. Zuo, C. S. Liu, W. Gao, D. J. Fu, *Appl. Surf. Sci.* **2020**, *506*, 145017.
[13] J. Asenbauer, A. Hoefling, S. Indris, J. Tübke, S. Passerini, D. Bresser, *ACS Appl. Mater. Interfaces* **2020**, *12*, 8206.
[14] G. Giuli, T. Eisenmann, D. Bresser, A. Trapananti, J. Asenbauer, F. Mueller, S. Passerini, *Materials (Basel)* **2018**, *11*, 49.
[15] F. Mueller, D. Geiger, U. Kaiser, S. Passerini, D. Bresser, *ChemElectroChem* **2016**, *3*, 1311.
[16] Y. Li, W. Li, M. Fang, X. Yao, C. Chen, M. Shui, J. Shu, Y. Ren, *Curr. Appl. Phys.* **2017**, *17*, 1050.
[17] L. Wang, K. Tang, M. Zhang, J. Xu, *Nanoscale Res. Lett.* **2015**, *10*, 280.
[18] T. Eisenmann, A. Birrozzi, A. Mullaliu, G. Giuli, A. Trapananti, S. Passerini, D. Bresser, Unpublished.
[19] J. Asenbauer, J. R. Binder, F. Mueller, M. Kuenzel, D. Geiger, U. Kaiser, S. Passerini, D. Bresser, *ChemSusChem* **2020**, *13*, 3504.
[20] M. V. Reddy, G. V. Subba Rao, B. V. R. R. Chowdari, *Chem. Rev.* **2013**, *113*, 5364.
[21] L. Li, *Synthesis and Electrochemical Studies of Nanostructured Metal Oxides for Lithium Ion Batteries*, Nanyang Technological University, Singapore **2016**.
[22] R. Hu, Y. Ouyang, T. Liang, X. Tang, B. Yuan, J. Liu, L. Zhang, L. Yang, M. Zhu, *Energy Environ. Sci.* **2017**, *10*, 2017.
[23] G. Giuli, A. Trapananti, F. Mueller, D. Bresser, F. Dácapito, S. Passerini, *Inorg. Chem.* **2015**, *54*, 9393.
[24] J.-H. Choy, E.-S. Jang, J.-H. Won, J.-H. Chung, D.-J. Jang, Y.-W. Kim, *Appl. Phys. Lett.* **2004**, *84*, 287.
[25] X.-G. Han, H.-Z. He, Q. Kuang, X. Zhou, X.-H. Zhang, T. Xu, Z.-X. Xie, L.-S. Zheng, *J. Phys. Chem. C* **2009**, *113*, 584.
[26] A. Kocjan, M. Logar, Z. Shen, *Sci. Rep.* **2017**, *7*, 2541.
[27] D. Wei, R. Dave, R. Pfeffer, *J. Nanoparticle Res.* **2002**, *4*, 21.
[28] D. Bresser, E. Paillard, P. Niehoff, S. Krueger, F. Mueller, M. Winter, S. Passerini, *ChemPhysChem* **2014**, *15*, 2177.
[29] R. Malini, U. Uma, T. Sheela, M. Ganesan, N. G. Renganathan, *Ionics (Kiel)*. **2009**, *15*, 301.
[30] P. Poizot, S. Laruelle, S. Grugeon, L. Dupont, J. M. Tarascon, *Nature* **2000**, *407*, 496.
[31] A. D. Pelton, *J. Phase Equilibria* **1991**, *12*, 42.
[32] D. Bresser, E. Paillard, R. Kloepsch, S. Krueger, M. Fiedler, R. Schmitz, D. Baither, M. Winter, S. Passerini, *Adv. Energy Mater.* **2013**, *3*, 513.